ACS Sustainable Chemistry & Engineering

pubs.acs.org/journal/ascecg

Research Article

Highly Efficient Nickel, Iron, and Nitrogen Codoped Carbon Catalysts Derived from Industrial Waste Petroleum Coke for Electrochemical CO_2 Reduction

Yang Gang, Fuping Pan, Yuhuan Fei, Zichen Du, Yun Hang Hu, and Ying Li*

Cite This: *ACS Sustainable Chem. Eng.* 2020, 8, 8840−8847

Read Online

ACCESS | Metrics & More | Article Recommendations | Supporting Information

ABSTRACT: Electrochemical CO_2 reduction reaction (ECO_2RR) is a potentially promising way of producing sustainable energy by converting CO_2 into fuels or useful chemicals using alternative power sources such as solar and wind. However, finding cheap and abundant materials with a high catalytic activity for CO_2 reduction is critical for future larger-scale applications of ECO_2RR. Herein, we used petroleum coke (PC), an industrial waste, as the carbon source for preparing highly efficient ECO_2RR catalysts. By doping nickel and nitrogen into oxidized PC (Ni−N-PC), an ∼97% Faradaic efficiency of CO production has been achieved with a current density of ∼18 mA/cm^2 at −0.8 V versus the reversible hydrogen electrode. By further doping iron into the Ni−N-PC catalyst (forming Fe/Ni−N-PC), a 90% Faradaic efficiency of CO and a 20 mA/cm^2 CO partial current density were achieved. The ECO_2RR performance of the above PC-based catalysts was comparable to that of traditional graphite-based catalysts, but the former is an industrial waste and costs little. Findings from this work provide insight into transfer of industrial waste into a carbon precursor under similar treatment to synthesize efficient ECO_2RR catalysts.

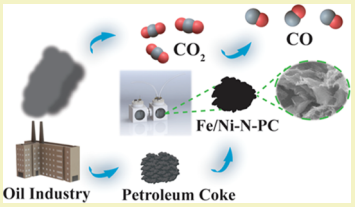

KEYWORDS: *Petroleum coke, Electrochemical CO_2 reduction, Industrial waste, CO selectivity*

INTRODUCTION

The increasing consumption of fossil fuels has led to increasing emissions of CO_2 that is believed to be the main cause for global warming. Electrochemical CO_2 reduction reaction (ECO_2RR), coupled with renewable energy sources such as solar and wind, is considered one of the most promising solutions to curb CO_2 emissions and generate useful chemicals simultaneously.[1,2] Among different pathways in the CO_2 reduction, the reduction of CO_2 to CO has been reported as the most viable and feasible reaction because of its lesser energy input and higher product yield and selectivity. The state-of-the-art catalysts to date that can efficiently reduce CO_2 to CO with high selectivity and activity are noble metals such as Au and Ag;[3,4] however, the high cost associated with noble metals prohibits large-scale applications of this process.

Carbon-based catalysts are recently reported to be a potential replacement to noble metals for ECO_2RR.[5−9] Studies have been focused on nitrogen-doped carbon catalysts with a trace of doped transition metals such as Ni, Fe, Co, and Zn that showed significantly improved activity and efficiency for ECO_2RR compared to metal-free carbon-based materials.[5,8,10−15] As a precursor, highly oxidized and functionalized carbon treated by oxidants is preferred because surface oxygen functional groups created from treatment will facilitate the metal- and nitrogen-doping process and create more metal−nitrogen−carbon active sites. After oxidation and doping, carbon materials as substrates can also provide higher surface areas for better contacting with CO_2 in the electrolyte. Traditional carbon materials used as catalyst supports include graphite, carbon black, and carbon nanotubes; however, their high costs prohibit large-scale applications.

Petroleum coke (PC), a waste product of the oil refining industry,[16] can be used as a cheap carbon precursor for applications such as a CO_2 sorbent,[17] water treatment,[18] and microbial fuel cells[19] because of its high content of carbon and low content of ash. To the best of our knowledge, there are very few reports on its application in electrochemical CO_2 reduction. As shown in Figure 1, the process of converting PC to a carbon catalyst for ECO_2RR uses a solid waste (PC) from the oil industry to manage another gaseous waste, CO_2, from the same industry. In other words, it converts both wastes into useful products.

However, as a carbon catalyst, raw PC suffers from several disadvantages including large particle size, small surface area, and too many useless impurities for CO_2 reduction such as Ca, Al, Na, and K, most importantly, the unfunctionalized pristine carbon surface making it harder for metal- and nitrogen-doping process. Therefore, like other pristine carbon materials (carbon black, graphite, or CNT), treatments to raw PC are also needed to meet the goal of efficient ECO_2RR. In this work, PC

Received: April 23, 2020
Published: May 19, 2020

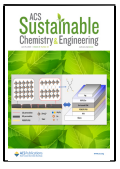

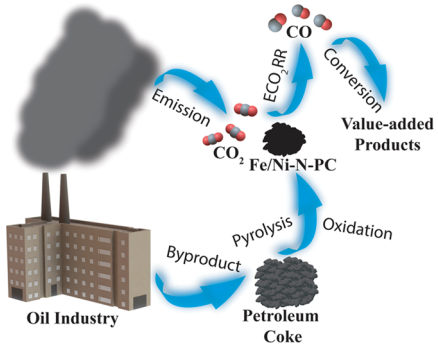

Figure 1. Schematic illustrating the process of utilizing industrial byproduct PC as an efficient catalyst for ECO_2RR.

had undergone oxidation pretreatment, followed by doping of a transition metal (e.g., Ni, Fe, or Ni/Fe) and nonmetal (e.g., N), and the resultant catalysts were evaluated for ECO_2RR. In addition, a benchmark catalyst using graphite as the precursor was also prepared and its performance compared with that made from PC. Similar ECO_2RR activities of the materials were observed, indicating the potential of PC as an alternative carbon precursor for the ECO_2RR process.

EXPERIMENTAL SECTION

Synthesis of Oxidized PC. The synthesis of oxidized PC (O-PC) follows a typical acid and oxidant treatment published in the previous report.[20] Thus, 0.75 g of raw PC was mixed with 4.5 g of $KMnO_4$, 90 mL of concentrated H_2SO_4, and 10 mL of $H_3(PO_4)_3$ in a round-bottom flask. The mixture was then placed in an oil bath and kept at 55 °C for 12 h. After that, the mixture was poured onto DI water-derived ice and 30% H_2O_2 was added until the color turned from purple to dark yellow. The mixture was then centrifuged and washed with 37% HCl/water/ethanol (volume ratio 1:1:1) twice and ethanol once. The powder was placed in a vacuum oven at room temperature and dried overnight.

Synthesis of Metal- and Nitrogen-Doped PC (Ni−N-PC or Fe−N-PC). O-PC (200 mg) was dispersed in 50 mL of ethanol in an ultrasonic bath for 15 min; 0.3 mmol $Ni(NO_3)_2{\cdot}6H_2O$ was dissolved in 50 mL of ethanol with ultrasonic dispersion and then added into the O-PC suspended solution, where Ni^{2+} was absorbed onto the O-PC surface. The mixture was stirred under room temperature for 4 h and then centrifuged and washed with ethanol twice to remove the solvent and additional metal salts. The powder of Ni-deposited O-PC (Ni/O-PC) was obtained by vacuum-drying overnight at room temperature. To dope nitrogen into the material, Ni/O-PC was mixed with 1 g of urea and treated at 900 °C in a tube furnace under an Ar flow of 80 sccm. The final catalyst is denoted as Ni−N-PC. Similarly, Fe−N-PC was prepared in the same process except for replacing 0.3 mmol $Ni(NO_3)_2{\cdot}6H_2O$ by 0.3 mmol $FeCl_3$.

Synthesis of Ni, Fe, and N Codoped PC (Fe/Ni−N-PC). Ni-deposited O-PC after centrifugation was dispersed into 20 mL of ethanol and sonicated for 15 min to mix uniformly. Ethanol dissolved with 1 mg of $FeCl_3$ was added into the mixture drop by drop. The as-prepared mixture was taken onto a hot plate to stir under 300 rpm at room temperature until the solvent fully evaporated. The powder after evaporation was collected and mixed with 1 g of urea and treated at 900 °C in a tube furnace under an Ar flow of 80 sccm. The final catalyst was collected after that and denoted as Fe/Ni−N-PC.

Synthesis of Metal- and Nitrogen-Doped Graphite (Fe−N-Gr or Ni−N-Gr). Ni- and N-doped graphite (Ni−N-Gr) was prepared under the same process as Ni−N-PC except for replacing PC by graphite. Fe- and N-doped graphite (Fe−N-Gr) was also prepared under the same process as Fe−N-PC. The graphite (Gr)- and PC-based catalysts have the same metal and nitrogen contents for comparison purposes.

Electrochemical CO_2RR Activity Measurements. ECO_2RR activity was measured in a two-compartment H-cell with a standard three-electrode system, as shown in Figure 2. An Ag/AgCl electrode

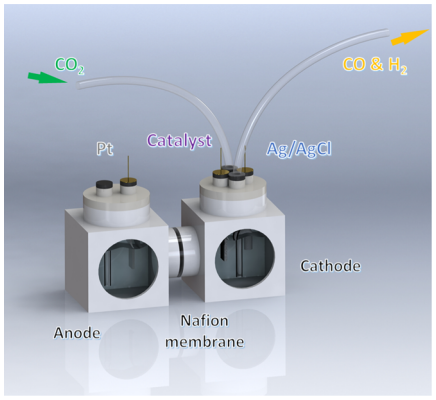

Figure 2. Schematic illustrating the H-cell configuration used in the electrocatalytic performance test.

filled with 3 M KCl and a Pt foil were used as the reference electrode and counter electrode, respectively. The measured potentials are recalculated by the following equation

$$\Delta E(\mathrm{RHE}) = E(\mathrm{Ag/AgCl}) + 0.210\ \mathrm{V} + 0.0591\ \mathrm{V} \times \mathrm{pH} \quad (1)$$

The working electrode was prepared by drop-casting the catalyst ink onto a Toray carbon paper with an active area of 1 cm^2. The catalyst mass loading was 1 mg/cm^2. The ink was prepared by dispersing 3 mg of the as-prepared catalyst in a mixture solution of 370 μL of ethanol, 200 μL of DI-water, and 30 μL of 5% Nafion solution under 3 h of sonication to achieve uniform catalyst dispersion.

The working electrode and reference electrode were placed into the cathode chamber, while the counter electrode was placed in the anode chamber. A CO_2-saturated 0.5 M $KHCO_3$ at pH 7.2 was used as the electrolyte. A piece of Nafion 115 proton exchange membrane (Fuel Cell Store, College Station, TX) was used to separate the two chambers in order to prevent the reoxidation of reduction-generated products. High-purity (99.999%) CO_2 was introduced into the cathode chamber for 1 h with a flow rate of 34 sccm (standard cubic centimeter per minute) to make a CO_2-saturated electrolyte before starting electrochemical tests. The electrolyte in the cathode chamber was stirred at 900 rpm during all the tests. The gas-phase products were analyzed via online gas chromatography (GC, Fuel Cell GC-2014ATF, Shimadzu) equipped with a thermal conductivity detector and a methanizer-assisted flame ionization detector. ^{1}H NMR spectra were obtained on a Bruker 400 MHz spectrometer. The catholyte was collected after 2 h of CO_2 reduction at −0.7 V versus reversible hydrogen electrode (RHE) for N-PC, Ni−N-PC, Fe−N-PC, and Fe/Ni−N-PC. 1,3,5-Trioxane was added to the catholyte as the internal standard. Then, the liquid sample was transferred to deuterated dimethyl sulfoxide and subjected to analysis.

The Faradaic efficiency (FE) of gaseous products at each applied potential was calculated based on the equation

$$\mathrm{FE} = (z{\cdot}P{\cdot}F{\cdot}V{\cdot}v_i)\ /(R{\cdot}T{\cdot}J) \quad (2)$$

where z is the number of electrons transferred per mole of gas product (z is 2 for CO and H_2), P is the pressure (1.01×10^5 Pa), F is the Faraday constant (96,500 $C{\cdot}mol^{-1}$), V is the gas volumetric flow rate (5.67×10^{-7} $m^3{\cdot}s^{-1}$), v_i is the volume concentration of the gas product determined by GC, R is the universal gas constant (8.314 J $mol^{-1}{\cdot}K^{-1}$), T is the temperature (298.15 K), and J is the steady-state current at each applied potential (A). v_i and J values for different groups are shown in Table S3 in the Supporting Information.

https://dx.doi.org/10.1021/acssuschemeng.0c03054
ACS Sustainable Chem. Eng. 2020, 8, 8840−8847

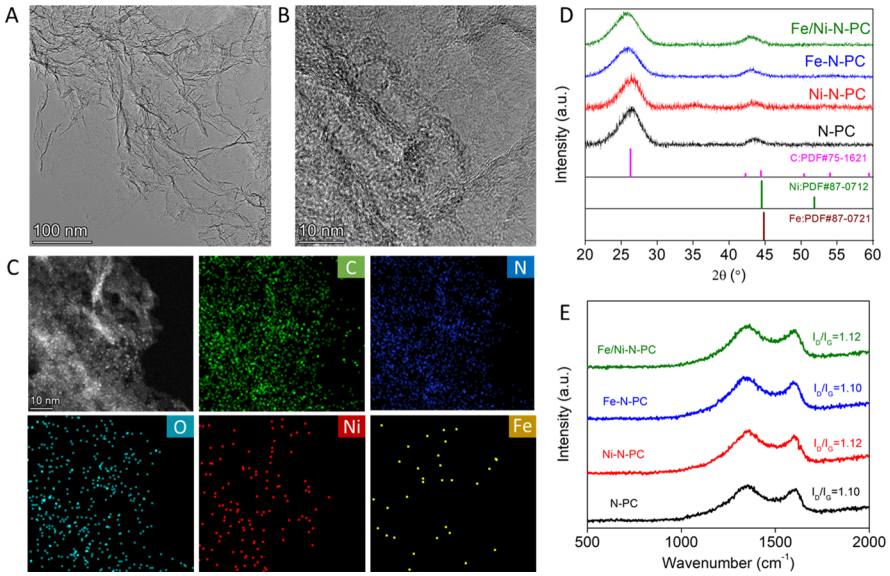

Figure 3. (A) TEM, (B) high-resolution TEM, and (C) EDS elemental mapping images of Fe/Ni−N-PC. (D) XRD patterns and (E) Raman spectra of different PC-based catalysts.

RESULTS AND DISCUSSION

Synthesis, Structure, and Composition Characterizations. The surface morphology of raw PC (Figure S1A) was characterized by scanning electron microscopy (SEM). Compared to the graphene sheets with a porous structure in Fe/Ni−N-PC as shown in Figure S1B, the particle size and surface morphology of PC have been changed after oxidation (Figure S1C) and thermal pyrolysis (Figure S1B). The red arrows in Figure S1B indicate the presence of pores on the surface of Fe/Ni−N-PC, while the raw PC in Figure S1A shows a large sheet-like morphology without a clear porous structure. The transmission electron microscopy (TEM) images in Figures 3A and S2 reveal a similar structure without large particulates in N-PC, Ni−N-PC, Fe−N-PC, and Fe/Ni−N-PC. The high-resolution TEM image in Figure 3B displays the layered carbon structure in Fe/Ni−N-PC, and the energy-dispersive X-ray spectroscopy (EDS) mapping in Figure 3C indicates the existence of homogenous distribution of C, N, O, Ni, and Fe species.

X-ray diffraction (XRD) and Raman spectroscopy were also conducted to determine the crystal structure of Ni−N-PC, Fe−N-PC, and Fe/Ni−N-PC catalysts. In Figure 3D, all the materials show broad peak patterns, indicating a low degree of crystallization. Two peaks at around 25.8 and 43° reflect the (002) and (100) planes of graphite-like carbons according to PDF#75-1621. All groups showed similar carbon peaks, indicating that metal doping does not affect the graphitization degree of carbon. Ni−N-PC catalysts prepared under different temperatures for screening the optimized pyrolysis temperature were also investigated, as shown in Figure S3; there are obvious Ni peaks at 44.5 and 51.8° in the group of Ni−N-PC under 1000 °C pyrolysis (PDF#87-0712), corresponding to Ni(111) and Ni(200). This indicates that the peak at 43° in all groups under 900 °C pyrolysis does not correspond to the metal peaks. No obvious metal peaks can be detected by XRD in N-PC, Ni−N-PC, Fe−N-PC, and Fe/Ni−N-PC, indicating that no bulk metal nanoparticles were formed during the pyrolysis or the concentration was too small to be detected by XRD. For Raman spectroscopy in Figure 3E, four groups with different metal dopings show similar vibrational bands centered at 1350 cm^{-1} (D band) and 1598 cm^{-1} (G band). The D band is referred to as the disorder-induced band and caused by the disorder structure of the graphene layer and the G band represents the bond stretching of sp^2 carbon. Typically, a higher band intensity ratio (I_D/I_G) shows more defects in the carbon structure.[21] The I_D/I_G ratio is very close for N-PC, Ni−N-PC, Fe−N-PC, and Fe/Ni−N-PC. They were calculated to be 1.10, 1.12, 1.10, and 1.12, respectively. This indicates that the defects on the carbon structure are similar for all materials.

Surface element compositions have been determined by X-ray photoelectron spectroscopy (XPS). It has been revealed by the XPS that the presentation of N 1s is at 400 eV, Ni $2p_{3/2}$ at 855 eV, and Fe $2p_{3/2}$ at 710 eV (Figure S4). The Ni peak positions of Ni−N-PC and Fe/Ni−N-PC are all located at ~855 eV, located differently compared with that of the Ni metal (Ni^0, 852.6 eV). The peak at 855 eV is close to that of Ni(OH)$_2$ (855.3 eV), indicating that Ni elements inside the catalyst occupy a Ni^{2+} oxidation state.[22] The Ni concentrations in Ni−N-PC and Fe/Ni−N-PC are 5 and 4.8 wt %, indicating a similar Ni-doping from a similar deposition preparation process. The Fe peak positions in Fe−N-PC and Fe/Ni−N-PC as shown in Figure S4 are located at 710 eV, located differently compared with that of the Fe metal (Fe^0, 706.7 eV). When both metal ions were absorbed at the same time by oxidized-PC, the performance of the as-prepared catalyst showed almost the same trend in FE(CO) and current density as the Fe^{3+} absorption group (Fe−N-PC). This is because Fe sites are more favorable to HER at more negative potentials, for example, −0.8 V versus RHE (Figure 5B). They will suppress the performance of Ni sites significantly toward ECO_2RR at higher overpotentials if too much Fe were deposited on the surface. As a result, dipping $FeCl_3$ solution into Ni-deposited oxidized-PC was used for group Fe/Ni−N-PC as shown in the Experimental Section to better control the concentration of Fe-doping and analyze the influence from Fe-doping to Ni active sites. Because of the above process, the deposition-prepared Fe−N-PC has a 4.7 wt % Fe concentration detected by XPS. However, dipping Fe into Ni-absorbed O-PC in Fe/Ni−N-PC results in 0.4 wt % Fe concentration. From ICP−MS results

https://dx.doi.org/10.1021/acssuschemeng.0c03054
ACS Sustainable Chem. Eng. 2020, 8, 8840−8847

shown in Table S4, the concentration of Fe and Ni is low at 0.2 and 0.05 wt %, respectively, in the PC. Table S4 also lists the concentrations Fe and Ni in the prepared catalysts by ICP−MS in comparison to the raw PC. After the pretreatment, washing, and pyrolysis steps, the Fe and Ni concentration decreased to 0.1 and 0.02 wt %, respectively, in N-PC. For the Fe-doped catalyst, Fe−N-PC, the Fe concentration increased to 2.2 wt %, 1 order of magnitude higher than that in PC. For the Ni-doped catalyst, Ni−N-PC, the Ni concentration increased to 3.9%, 2 orders of magnitude higher than that in PC. The concentrations measured by ICP−MS match well with those detected by XPS, as shown in Table S1.

The N concentrations were calculated to be 10.2, 8.4, 6.7, and 7.9 wt % for N-PC, Ni−N-PC, Fe−N-PC, and Fe/Ni−N-PC, respectively (Table S1). This indicates a similar N-doping level in all the groups. This is probably because N-doping is mostly determined by both carbon and nitrogen precursors and the pyrolysis temperature.[23] High-resolution XPS spectra of N to determine the configuration of N dopants were further analyzed. For N 1s spectra (Figure 4A), they are fitted by four

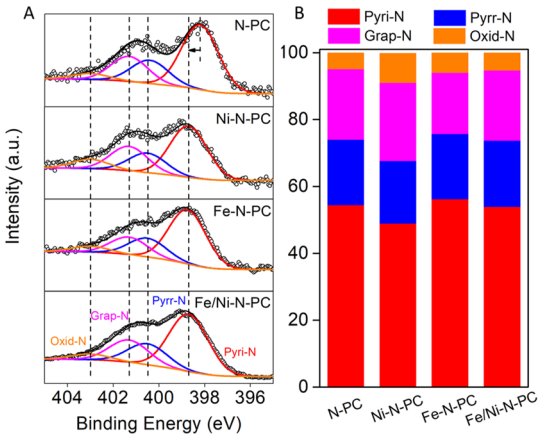

Figure 4. (A) High-resolution N 1s XPS spectra and (B) distribution of N dopants for the prepared catalyst materials.

curves centered at ∼398.2 eV for pyridinic N, ∼400.5 eV for pyrrolic N, ∼401.3 eV for graphitic N, and ∼403 eV for oxidized-like N species, respectively.[8,12,24] It has been previously demonstrated that the electronic environment of N atoms in M−N−C could be altered as compared with metal-free N−C.[25,26] This change can be directly verified by comparing N 1s spectra of different groups, which is a tool widely used to verify the generation of metal-N species.[27−29] It can be seen that the pyridinic-N position in N-PC centered at 398.2 eV is positively shifted to 398.7 eV in Ni−N-PC, Fe−N-PC, and Fe/Ni−N-PC with a binding energy increase of 0.5 eV in Figure 4A, whereas the other three N species showed no position difference between metal-doped and metal-free groups. This positive shift of pyridinic N can be attributed to the bonding formation between metal and pyridinic N atoms. The findings here agree with the previous literature that the binding energy of pyridinic N will shift to a higher value when a chemical bonding is formed between the metal and N atoms.[8,28,30] In addition, pyridinic N dominates in the N compositions of all groups by more than 50% calculated by the fitting peak areas, as shown in Figure 4B. The graphitic N percentage is similar among all the groups.

However, the explicit coordination environment of Ni or Fe is still not clear. For example, one previous work[31] reported a NiN_4C_4 moiety with one oxygen atom in the axial direction, which means that a metal could be also bonded with an O atom together with four N atoms. However, the oxygen functional group in the oxidized carbon is not very stable under high-temperature pyrolysis, especially with the presence of the N-source. These N-containing precursors would release N-containing gases such as NH_3 during the pyrolysis, reducing oxidized carbon back to carbon while doping nitrogen onto the carbon lattice at the same time.[32] As a result, though the exact structure of M−N−C is still unclear, it is generally accepted that most of the metal species are more likely to be bonded with nitrogen. A small portion of metal bonding with either carbon or oxygen may also exist based on previous reports.

High-angle angular dark-field scanning transmission electron microscopy (HAADF-STEM) was also conducted to examine the structure of metal sites. As shown in Figure 5A, N-PC

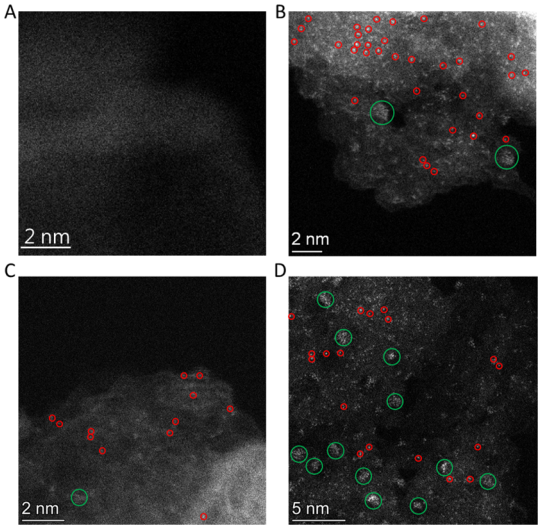

Figure 5. HAADF-STEM images of (A) N-PC, (B) Ni−N-PC, (C) Fe−N-PC, and (D) Fe/Ni−N-PC.

displays no bright spots, indicating no metal sites in the "metal-free" control group. Compared with N-PC, Ni−N-PC (Figure 5B) shows densely dispersed bright spots corresponding to Ni atoms (red circles). Notably, Ni−N-PC is not a perfect single-atomic catalyst because nanoclusters could also be observed as outlined in green circles. Fe−N-PC (Figure 5C) also displays bright dots, indicating the existence of single Fe sites in the carbon lattice. Fe/Ni−N-PC (Figure 5D) shows a combination of single-atomic sites and nanocluster sites, and it displays more nanocluster sites than Ni−N-PC. These nanoclusters could be a combination of Ni and Fe metals because of the double-metal doping processes, which, however, cannot be directly confirmed from the HAADF-STEM image. The ratio of single atomic sites to nanoclusters (less than 2 nm) was then estimated by a statistic method.[33] Compared to Ni−N-PC with only 1.5% of total sites being nanoclusters, Fe/Ni−N-PC showed 9% (Figure S5).

Electrochemical CO_2 Reduction Performance. Linear sweep voltammetry (LSV) was first assessed, as shown in Figure 6A. When the applied potential was more negative than −0.4 V versus RHE, the current density of Ni/Fe−N-PC increased more quickly in the CO_2-saturated electrolyte than

https://dx.doi.org/10.1021/acssuschemeng.0c03054
ACS Sustainable Chem. Eng. 2020, 8, 8840−8847

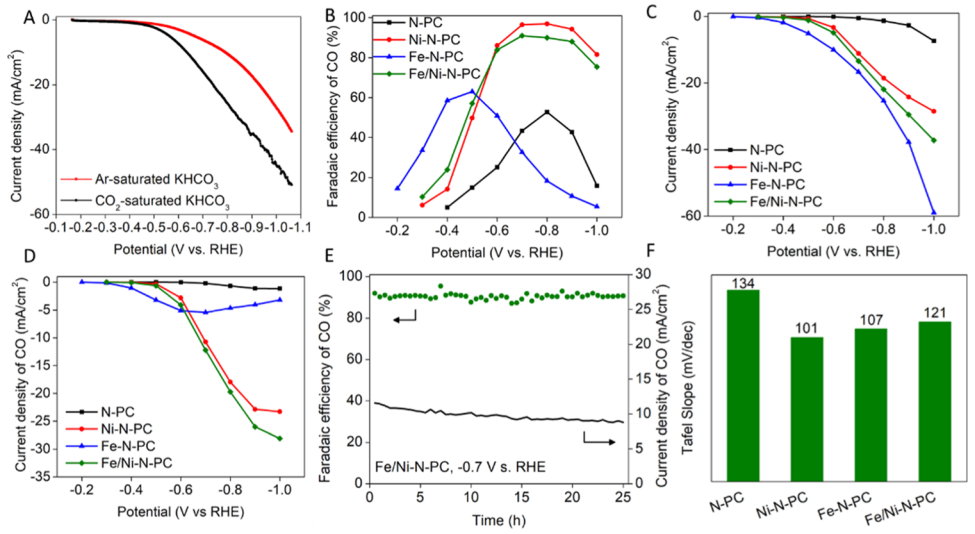

Figure 6. (A) LSV curves recorded on Fe/Ni−N-PC in the Ar- and CO_2-saturated 0.5 M $KHCO_3$ solution at a scan rate of 5 mV·s^{-1}, (B) CO FEs, (C) total current density, (D) CO partial current density of groups with different metal dopants, (E) chronoamperometric response and CO FEs at −0.7 V on Fe/Ni−N-PC for stability tests, and (F) Tafel slopes for CO production.

the Ar-saturated one. This indicates the occurrence of ECO_2RR together with hydrogen evolution reaction (HER), as there is still activity in the Ar-saturated electrolyte. To further investigate the product selectivity, CO_2 reduction was carried out in a constant potential test mode. CO and H_2 were detected as the main gaseous products by GC, and no other products were observed. No HCOOH could be detected by ^{1}H NMR for each group, as shown in Figure S6, indicating that no liquid product was produced during the electrolysis. At each potential, the FE(CO) data are shown in Figure 6B, total current density in Figure 6C, and CO partial current density in Figure 6D. The metal-free group N-PC showed its highest FE of CO at −0.8 V versus RHE. The CO selectivity is 52% and the current density is 0.7 mA/cm^2. Compared with the metal-free group, both Fe-doped and Ni-doped groups performed with much larger current densities. Fe−N-PC reaches the highest FE, 63% at −0.5 V versus RHE, with a CO current density of 3.2 mA/cm^2. This indicates that by doping Fe, the overpotential for reaching the maximum CO FE can be reduced. Fe doping triggers the reduction reaction at a lower potential from −0.2 to −0.5 V. However, H_2 generation dominates at potentials more negative than −0.6 V. Ni−N-PC showed a different selectivity trend to Fe−N-PC. It has the highest FE(CO), 97%, at −0.8 V versus RHE, with a CO current density of 18 mA/cm^2. From the results, Ni doping does not reduce the overpotential for reaching maximum FE(CO) but can achieve a much higher selectivity and larger current density at the same potential than the metal-free group. At potentials more negative than −0.5 V, CO dominates in the products, making Ni doping advantageous in compressing H_2 generation at larger overpotentials. The hybrid system Fe/Ni−N-PC showed its highest FE(CO) of 91% at −0.7 V with a CO current density of 12.2 mA/cm^2. The CO current density of the hybrid group at −0.8 V is 20 mA/cm^2, larger than 18 mA/cm^2 from Ni−N-PC. These results indicate that the potential for reaching the highest CO selectivity can be shifted from −0.8 to −0.7 V by adding Fe into the system. The electrocatalytic performance of Fe/Ni-N-PC reveals that by adding Fe together with Ni-doping, the ECO_2RR activity can be enhanced at all the potentials with only a small extent of loss on FE at potentials more negative than −0.6 V versus RHE (maximum loss from 97 to 90% at −0.8 V). These results agree with the HAADF-STEM observation on Fe/Ni sites and the electrocatalytic performance on Fe/Ni sites in the literature.[5,8,12,34−36] It is easier for metal nanoclusters and larger particles to generate H_2 than single atomic sites as reported in the literature,[37] which agrees with the electrocatalytic performance in Figure 6B where Ni−N-PC shows a higher FE of CO than Fe/Ni−N-PC at −0.8 V versus RHE.

In addition, the long-term electrochemical stability of Fe/Ni−N-PC was investigated at the potential of −0.7 V versus RHE where the maximum FE(CO) was performed. As indicated in Figure 6E, the current density underwent only a slight decrease (less than 20%) in the 24 h stability test. In addition, the FE(CO) remained stable and above 90% during the 24 h test. Furthermore, the performances of PC-based catalysts developed in this work are compared with those in the literature reports, as shown in Table S2. The performances of our materials are comparable to or higher than those reported in the literature, but we used low-cost PC, while others used more expensive carbon precursors. Tafel plots (Figures S3D and 6F) showed the Tafel slope of 101 mV·dec^{-1}. N-PC, Fe−N-PC, and Fe/Ni−N-PC showed 134, 107, and 121 mV·dec^{-1}, respectively. All Tafel slopes were close to the theoretical value, 118 mV·dec^{-1}, which indicates that the reaction rate of CO_2 reduction is determined by the step of forming *COOH intermediates through the initial single electron transfer.[38]

The Nyquist plots by electrochemical impedance spectroscopy were obtained as in Figure S7A, and the equivalent circuit model in the cathode compartment was defined as in Figure S7B. In the equivalent circuit model, R_S represents the solution resistance, which could be assigned to the intercept on the real axis in Nyquist plots. The first semicircle was usually assigned as the Ohmic resistance R_Ω, representing the conductivity of the catalysts. The third resistance is assigned as the charge-transfer resistance (R_{CT}), representing the resistance for the electrons to transfer from the catalyst to the reactants. Q_1 and Q_2 represent the constant phase element, corresponding to the capacitance together with each resistance.[39,40] The fitting results are shown in Table S5. All groups have a similar

https://dx.doi.org/10.1021/acssuschemeng.0c03054
ACS Sustainable Chem. Eng. 2020, 8, 8840−8847

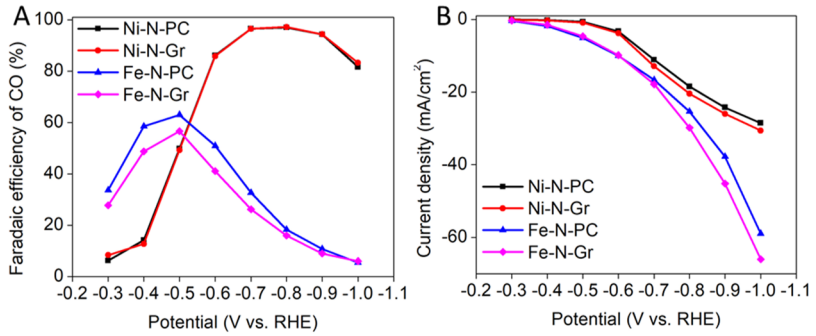

Figure 7. (A) CO FEs and (B) total current density of Ni−N-PC, Ni−N-Gr, Fe−N-PC, and Fe−N-Gr.

solution resistance (R_S = ∼1.5 Ω) as well as Ohmic resistance (R_Ω = 2−3 Ω). This agrees with the Raman spectroscopy that conductivities of the catalysts are similar. However, the "metal-free" group N-PC shows a significantly higher charge-transfer resistance (R_{CT}) than any other groups with metal doping, suggesting that the M−N active site formation accelerates the electron transfer. All the groups with metal doping showed a similar charge-transfer resistance (R_{CT} = 6−8 Ω), suggesting that different metal/anion configurations play a similar role to the resistance of the system.

The electrochemical surface area via double-layer capacitance (C_{dl}) using cyclic voltammograms was measured, as shown in Figures S8 and S9. Fe/Ni−N-PC and Fe−N-PC showed larger C_{dl} than N-PC and Ni−N-PC, which could result in more potential electrical active sites. This is a trend similar to the literature report.[41]

Activity Comparison between the PC-Based Catalyst and the Traditional Gr-Based Catalyst. Performance comparisons between the PC-based and graphite-based catalysts were carried out as well to further demonstrate the cost-effectiveness of the PC-based catalysts. Ni−N-Gr and Fe−N-Gr represents the catalysts prepared by the oxidized graphite through the same synthesis process as Ni−N-PC and Fe−N-PC. Figure 7A compares the FE(CO) for the two types of catalysts. It shows that Ni−N-PC has an almost identical FE(CO) distribution to that of Ni−N-Gr; both had 97% CO selectivity at −0.8 V versus RHE. However, for the Fe-doped catalysts, the Fe−N-PC catalyst had an even higher CO selectivity than that of Fe−N-Gr at all potentials. Figure 7B compares the total current density of the two catalysts. Both Ni−N-Gr and Fe−N-Gr had a slightly larger total current density than their counterpart of Ni−N-PC and Fe−N-PC. The overall considerations of total current density and CO selectivity reveal a comparable performance between the two types of catalysts, suggesting that PC-based catalysts are cost-effective.

XRD and Raman spectroscopy were also carried out to compare the materials' properties of PC- and graphite-based catalysts (Ni−N-PC, Ni−N-Gr, Fe−N-PC, and Fe−N-Gr), and the results are shown in Figures S10A (XRD) and S10B (Raman). The PC-based catalysts demonstrated similar diffraction peaks in XRD and very close I_D/I_G ratio in Raman to those of graphite-based catalysts. The similar catalytic activity and lower cost of PC suggest a feasible pathway toward large-scale synthesis of cost-effective ECO_2RR catalysts.

CONCLUSIONS

In summary, we demonstrated the transformation of an industrial waste, PC, into an efficient catalyst for ECO_2RR by additional Ni, Fe, and N doping in the carbon lattice. Ni- and N-doped active sites can significantly improve the CO selectivity and current density of CO_2 reduction. Ni- and N-doped PC (Ni−N-PC) achieved 97% FE of CO at −0.8 V versus RHE. With further Fe doping into Ni−N-PC (forming Fe/Ni−N-PC), the electrochemical active surface area could be increased. The maximum FE of CO (91%) in Fe/Ni−N-PC was achieved at a lower overpotential (−0.7 V). In addition, the bimetal doping of Ni and Fe enhanced both the total current density and CO partial current density at all potentials from −0.3 to −1 V. The cost-effectiveness of PC-based catalysts was evaluated by comparing their catalytic performance with those of graphite-based materials synthesized in the same process. PC-based materials showed a comparable current density and CO selectivity to those of graphite-base materials, indicating the potential of fabricating efficient catalysts for ECO_2RR from abundant industrial wastes.

ASSOCIATED CONTENT

Supporting Information

The Supporting Information is available free of charge at https://pubs.acs.org/doi/10.1021/acssuschemeng.0c03054.

Characterization methods and equipment; SEM images, additional TEM and HAADF-STEM images, additional electrocatalytic performance for Ni−N-PC under different temperatures, XPS survey spectra, ^{1}H NMR analysis for liquid product, CV curves analyzing ESCA, and XRD and Raman spectra for graphite-based materials; element concentrations by XPS, performance comparison against previous reports, and product concentration detected by GC; and current measured by the electrochemical station and metal impurity concentration measured by ICP−MS (PDF)

AUTHOR INFORMATION

Corresponding Author

Ying Li − *J. Mike Walker '66 Department of Mechanical Engineering, Texas A&M University, College Station, Texas 77843, United States;* orcid.org/0000-0002-6775-5649; Email: yingli@tamu.edu

Authors

Yang Gang − *J. Mike Walker '66 Department of Mechanical Engineering, Texas A&M University, College Station, Texas 77843, United States*

https://dx.doi.org/10.1021/acssuschemeng.0c03054
ACS Sustainable Chem. Eng. 2020, 8, 8840−8847

Fuping Pan − *J. Mike Walker '66 Department of Mechanical Engineering, Texas A&M University, College Station, Texas 77843, United States;* orcid.org/0000-0001-9171-0726
Yuhuan Fei − *Department of Materials Science and Engineering, Michigan Technological University, Houghton, Michigan 49931-1295, United States*
Zichen Du − *J. Mike Walker '66 Department of Mechanical Engineering, Texas A&M University, College Station, Texas 77843, United States*
Yun Hang Hu − *Department of Materials Science and Engineering, Michigan Technological University, Houghton, Michigan 49931-1295, United States;* orcid.org/0000-0002-5358-8667

Complete contact information is available at: https://pubs.acs.org/10.1021/acssuschemeng.0c03054

Notes

The authors declare no competing financial interest.

■ ACKNOWLEDGMENTS

This work was supported by the American Chemical Society Petroleum Research Fund (ACS-PRF, grant no. 58167-ND10) and U.S. National Science Foundation (NSF CBET #1805132). The use of the Texas A&M University Materials Characterization Facility is also acknowledged.

■ REFERENCES

(1) Zheng, T.; Jiang, K.; Wang, H. Recent Advances in Electrochemical CO2 -to-CO Conversion on Heterogeneous Catalysts. *Adv. Mater.* **2018**, *30*, 1802066.
(2) Liu, M.; Pang, Y.; Zhang, B.; De Luna, P.; Voznyy, O.; Xu, J.; Zheng, X.; Dinh, C. T.; Fan, F.; Cao, C.; de Arquer, F. P. G.; Safaei, T. S.; Mepham, A.; Klinkova, A.; Kumacheva, E.; Filleter, T.; Sinton, D.; Kelley, S. O.; Sargent, E. H. Enhanced electrocatalytic CO2 reduction via field-induced reagent concentration. *Nature* **2016**, *537*, 382.
(3) Lu, Q.; Rosen, J.; Zhou, Y.; Hutchings, G. S.; Kimmel, Y. C.; Chen, J. G. G.; Jiao, F. A selective and efficient electrocatalyst for carbon dioxide reduction. *Nat. Commun.* **2014**, *5*, 3242.
(4) Zhu, W.; Michalsky, R.; Metin, Ö.; Lv, H.; Guo, S.; Wright, C. J.; Sun, X.; Peterson, A. A.; Sun, S. Monodisperse Au Nanoparticles for Selective Electrocatalytic Reduction of CO2 to CO. *J. Am. Chem. Soc.* **2013**, *135*, 16833−16836.
(5) Pan, F.; Zhang, H.; Liu, K.; Cullen, D.; More, K.; Wang, M.; Feng, Z.; Wang, G.; Wu, G.; Li, Y. Unveiling Active Sites of CO2 Reduction on Nitrogen-Coordinated and Atomically Dispersed Iron and Cobalt Catalysts. *ACS Catal.* **2018**, *8*, 3116−3122.
(6) Pan, F.; Li, B.; Xiang, X.; Wang, G.; Li, Y. Efficient CO2 Electroreduction by Highly Dense and Active Pyridinic Nitrogen on Holey Carbon Layers with Fluorine Engineering. *ACS Catal.* **2019**, *9*, 2124−2133.
(7) Pan, F.; Zhao, H.; Deng, W.; Feng, X.; Li, Y. A novel N,Fe-Decorated carbon nanotube/carbon nanosheet architecture for efficient CO2 reduction. *Electrochim. Acta* **2018**, *273*, 154−161.
(8) Pan, F.; Deng, W.; Justiniano, C.; Li, Y. Identification of champion transition metals centers in metal and nitrogen-codoped carbon catalysts for CO2 reduction. *Appl. Catal. B Environ.* **2018**, *226*, 463−472.
(9) Zhang, C.; Yang, S.; Wu, J.; Liu, M.; Yazdi, S.; Ren, M.; Sha, J.; Zhong, J.; Nie, K.; Jalilov, A. S.; Li, Z.; Li, H.; Yakobson, B. I.; Wu, Q.; Ringe, E.; Xu, H.; Ajayan, P. M.; Tour, J. M. Electrochemical CO2 Reduction with Atomic Iron-Dispersed on Nitrogen-Doped Graphene. *Adv. Energy Mater.* **2018**, *8*, 1703487.
(10) Liu, S.; Yang, H.; Huang, X.; Liu, L.; Cai, W.; Gao, J.; Li, X.; Zhang, T.; Huang, Y.; Liu, B. Identifying Active Sites of Nitrogen-Doped Carbon Materials for the CO2 Reduction Reaction. *Adv. Funct. Mater.* **2018**, *28*, 1800499.
(11) Genovese, C.; Schuster, M. E.; Gibson, E. K.; Gianolio, D.; Posligua, V.; Grau-Crespo, R.; Cibin, G.; Wells, P. P.; Garai, D.; Solokha, V.; Krick Calderon, S.; Velasco-Velez, J. J.; Ampelli, C.; Perathoner, S.; Held, G.; Centi, G.; Arrigo, R. Operando spectroscopy study of the carbon dioxide electro-reduction by iron species on nitrogen-doped carbon. *Nat. Commun.* **2018**, *9*, 935.
(12) Zheng, T.; Jiang, K.; Ta, N.; Hu, Y.; Zeng, J.; Liu, J.; Wang, H. Large-Scale and Highly Selective CO2 Electrocatalytic Reduction on Nickel Single-Atom Catalyst. *Joule* **2019**, *3*, 265−278.
(13) Cheng, Y.; Zhao, S.; Li, H.; He, S.; Veder, J.-P.; Johannessen, B.; Xiao, J.; Lu, S.; Pan, J.; Chisholm, M. F.; Yang, S.-Z.; Liu, C.; Chen, J. G.; Jiang, S. P. Unsaturated edge-anchored Ni single atoms on porous microwave exfoliated graphene oxide for electrochemical CO2. *Appl. Catal. B Environ.* **2019**, *243*, 294−303.
(14) Lu, P.; Yang, Y.; Yao, J.; Wang, M.; Dipazir, S.; Yuan, M.; Zhang, J.; Wang, X.; Xie, Z.; Zhang, G. Facile synthesis of single-nickel-atomic dispersed N-doped carbon framework for efficient electrochemical CO2 reduction. *Appl. Catal. B Environ.* **2019**, *241*, 113−119.
(15) Yang, F.; Song, P.; Liu, X.; Mei, B.; Xing, W.; Jiang, Z.; Gu, L.; Xu, W. Highly Efficient CO2 Electroreduction on ZnN4 -based Single-Atom Catalyst. *Angew. Chem., Int. Ed.* **2018**, *57*, 12303−12307.
(16) Shi, Y.; Chen, J.; Chen, J.; Macleod, R. A.; Malac, M. Preparation and evaluation of hydrotreating catalysts based on activated carbon derived from oil sand petroleum coke. *Appl. Catal., A* **2012**, *441*−*442*, 99−107.
(17) Bai, R.; Yang, M.; Hu, G.; Xu, L.; Hu, X.; Li, Z.; Wang, S.; Dai, W.; Fan, M. A new nanoporous nitrogen-doped highly-efficient carbonaceous CO2 sorbent synthesized with inexpensive urea and petroleum coke. *Carbon* **2015**, *81*, 465−473.
(18) Zhang, D.; Yin, J.; Zhao, J.; Zhu, H.; Wang, C. Adsorption and removal of tetracycline from water by petroleum coke-derived highly porous activated carbon. *Int. J. Chem. Environ. Eng.* **2015**, *3*, 1504−1512.
(19) Zhang, P.; Liu, X.-H.; Li, K.-X.; Lu, Y.-R. Heteroatom-doped highly porous carbon derived from petroleum coke as efficient cathode catalyst for microbial fuel cells. *Int. J. Hydrogen Energy* **2015**, *40*, 13530−13537.
(20) Marcano, D. C.; Kosynkin, D. V.; Berlin, J. M.; Sinitskii, A.; Sun, Z.; Slesarev, A.; Alemany, L. B.; Lu, W.; Tour, J. M. Improved Synthesis of Graphene Oxide. *ACS Nano* **2010**, *4*, 4806−4814.
(21) Ferrari, A. C.; Basko, D. M. Raman spectroscopy as a versatile tool for studying the properties of graphene. *Nat. Nanotechnol.* **2013**, *8*, 235−246.
(22) Grosvenor, A. P.; Biesinger, M. C.; Smart, R. S. C.; McIntyre, N. S. New interpretations of XPS spectra of nickel metal and oxides. *Surf. Sci.* **2006**, *600*, 1771−1779.
(23) Sheng, Z.-H.; Shao, L.; Chen, J.-J.; Bao, W.-J.; Wang, F.-B.; Xia, X.-H. Catalyst-free synthesis of nitrogen-doped graphene via thermal annealing graphite oxide with melamine and its excellent electrocatalysis. *ACS Nano* **2011**, *5*, 4350−4358.
(24) Wang, H.; Yin, F. X.; Liu, N.; Kou, R. H.; He, X. B.; Sun, C. J.; Chen, B. H.; Liu, D. J.; Yin, H. Q. Engineering Fe-Fe 3 C@Fe-N-C Active Sites and Hybrid Structures from Dual Metal-Organic Frameworks for Oxygen Reduction Reaction in H 2 -O 2 Fuel Cell and Li-O 2 Battery. *Adv. Funct. Mater.* **2019**, *29*, 1901531.
(25) Wu, G.; Johnston, C. M.; Mack, N. H.; Artyushkova, K.; Ferrandon, M.; Nelson, M.; Lezama-Pacheco, J. S.; Conradson, S. D.; More, K. L.; Myers, D. J.; Zelenay, P. Synthesis-structure-performance correlation for polyaniline-Me-C non-precious metal cathode catalysts for oxygen reduction in fuel cells. *J. Mater. Chem.* **2011**, *21*, 11392−11405.
(26) Liang, H.-W.; Wei, W.; Wu, Z.-S.; Feng, X.; Müllen, K. Mesoporous Metal-Nitrogen-Doped Carbon Electrocatalysts for Highly Efficient Oxygen Reduction Reaction. *J. Am. Chem. Soc.* **2013**, *135*, 16002−16005.
(27) Salavati-Niasari, M.; Amiri, A. Synthesis and characterization of alumina-supported Mn (II), Co (II), Ni (II) and Cu (II) complexes of bis (salicylaldiminato) hydrazone as catalysts for oxidation of

cyclohexene with tert-buthylhydroperoxide. *Appl. Catal., A* **2005**, *290*, 46−53.
(28) Li, X.; Bi, W.; Chen, M.; Sun, Y.; Ju, H.; Yan, W.; Zhu, J.; Wu, X.; Chu, W.; Wu, C.; Xie, Y. Exclusive Ni-N4 Sites Realize Near-Unity CO Selectivity for Electrochemical CO2 Reduction. *J. Am. Chem. Soc.* **2017**, *139*, 14889−14892.
(29) Cui, X.; Yang, S.; Yan, X.; Leng, J.; Shuang, S.; Ajayan, P. M.; Zhang, Z. Pyridinic-Nitrogen-Dominated Graphene Aerogels with Fe-N-C Coordination for Highly Efficient Oxygen Reduction Reaction. *Adv. Funct. Mater.* **2016**, *26*, 5708−5717.
(30) Fei, H.; Dong, J.; Arellano-Jiménez, M. J.; Ye, G.; Kim, N. D.; Samuel, E. L.; Peng, Z.; Zhu, Z.; Qin, F.; Bao, J. Atomic cobalt on nitrogen-doped graphene for hydrogen generation. *Nat. Commun.* **2015**, *6*, 8668.
(31) Fei, H.; Dong, J.; Feng, Y.; Allen, C. S.; Wan, C.; Volosskiy, B.; Li, M.; Zhao, Z.; Wang, Y.; Sun, H.; An, P.; Chen, W.; Guo, Z.; Lee, C.; Chen, D.; Shakir, I.; Liu, M.; Hu, T.; Li, Y.; Kirkland, A. I.; Duan, X.; Huang, Y. General synthesis and definitive structural identification of MN4C4 single-atom catalysts with tunable electrocatalytic activities. *Nat. Catal.* **2018**, *1*, 63−72.
(32) Li, X.; Wang, H.; Robinson, J. T.; Sanchez, H.; Diankov, G.; Dai, H. Simultaneous nitrogen doping and reduction of graphene oxide. *J. Am. Chem. Soc.* **2009**, *131*, 15939−15944.
(33) Akri, M.; Zhao, S.; Li, X.; Zang, K.; Lee, A. F.; Isaacs, M. A.; Xi, W.; Gangarajula, Y.; Luo, J.; Ren, Y. Atomically dispersed nickel as coke-resistant active sites for methane dry reforming. *Nat. Commun.* **2019**, *10*, 1−10.
(34) Pan, F.; Li, B.; Sarnello, E.; Hwang, S.; Gang, Y.; Feng, X.; Xiang, X.; Adli, N. M.; Li, T.; Su, D. Boosting CO2 Reduction on Fe-NC with Sulfur Incorporation: Synergistic Electronic and Structural Engineering. *Nano Energy* **2019**, *68*, 104384.
(35) Pan, F.; Zhang, H.; Liu, Z.; Cullen, D.; Liu, K.; More, K.; Wu, G.; Wang, G.; Li, Y. Atomic-level active sites of efficient imidazolate framework-derived nickel catalysts for CO2 reduction. *J. Mater. Chem. A* **2019**, *7*, 26231−26237.
(36) Möller, T.; Ju, W.; Bagger, A.; Wang, X.; Luo, F.; Ngo Thanh, T.; Varela, A. S.; Rossmeisl, J.; Strasser, P. Efficient CO2 to CO electrolysis on solid Ni-N-C catalysts at industrial current densities. *Energy Environ. Sci.* **2019**, *12*, 640−647.
(37) Huan, T. N.; Ranjbar, N.; Rousse, G.; Sougrati, M.; Zitolo, A.; Mougel, V.; Jaouen, F.; Fontecave, M. Electrochemical Reduction of CO2 Catalyzed by Fe-N-C Materials: A Structure-Selectivity Study. *ACS Catal.* **2017**, *7*, 1520−1525.
(38) Xie, J.; Zhao, X.; Wu, M.; Li, Q.; Wang, Y.; Yao, J. Metal-Free Fluorine-Doped Carbon Electrocatalyst for CO2 Reduction Outcompeting Hydrogen Evolution. *Angew. Chem., Int. Ed.* **2018**, *57*, 9640−9644.
(39) Won, D. H.; Shin, H.; Koh, J.; Chung, J.; Lee, H. S.; Kim, H.; Woo, S. I. Highly Efficient, Selective, and Stable CO 2 Electroreduction on a Hexagonal Zn Catalyst. *Angew. Chem., Int. Ed.* **2016**, *55*, 9297−9300.
(40) Pan, F.; Li, B.; Deng, W.; Du, Z.; Gang, Y.; Wang, G.; Li, Y. Promoting electrocatalytic CO2 reduction on nitrogen-doped carbon with sulfur addition. *Appl. Catal. B Environ.* **2019**, *252*, 240−249.
(41) Ju, W.; Bagger, A.; Hao, G.-P.; Varela, A. S.; Sinev, I.; Bon, V.; Cuenya, B. R.; Kaskel, S.; Rossmeisl, J.; Strasser, P. Understanding activity and selectivity of metal-nitrogen-doped carbon catalysts for electrochemical reduction of CO 2. *Nat. Commun.* **2017**, *8*, 1−9.

https://dx.doi.org/10.1021/acssuschemeng.0c03054
ACS Sustainable Chem. Eng. 2020, 8, 8840−8847